

# Binary Black Hole Accretion Flows in Merged Galactic Nuclei

Kimitake HAYASAKI

*Yukawa Institute for Theoretical Physics,  
 Oiwake-cho, Kitashirakawa, Sakyo-ku, Kyoto 606-8502  
 kimitake@yukawa.kyoto-u.ac.jp*

Shin MINESHIGE

*Yukawa Institute for Theoretical Physics,  
 Oiwake-cho, Kitashirakawa, Sakyo-ku, Kyoto 606-8502  
 and  
 Hiroshi SUDOU*

*Faculty of Engineering, Gifu University, Gifu 501-1193*

(Received 2006 September 6; accepted 2006 0)

## Abstract

We study the accretion flows from the circumbinary disks onto the supermassive binary black holes in a subparsec scale of the galactic center , using a smoothed particles hydrodynamics (SPH) code. Simulation models are presented in four cases of a circular binary with equal masses and unequal masses, and of an eccentric binary with equal masses and unequal masses. We find that the circumbinary disks are formed around each black holes regardless of simulation parameters. There are two-stage mechanisms to cause an accretion flow from the circumbinary disk onto supermassive binary black holes: First, the tidally induced elongation of the circumbinary disk triggers mass inflow towards two points on the semi-minor axis of circumbinary disk. Then, the gas is increasingly accumulated on these two points owing to the gravitational attraction of black holes. Second, when the gas can pass across the maximum loci of the binary potential, it starts to overflow via their two points and freely infalls to each black hole. In circular binaries, the gas continues to be supplied from the circumbinary disk (i.e. the gap between the circumbinary disk and the binary black hole is always closed.) In eccentric binaries, there is the mass supply with the periodic on/off transitions during one orbital period because of the time-dependent, periodic potential. The gap starts to close after the apastron and to open again after the next periastron passage. Due to this gap closing/opening cycles, the mass-capture rates are eventually strongly phase dependent. This could provide observable diagnosis for the presence of supermassive binary black holes in merged galactic nuclei.

**Key words:** black hole physics – accretion, accretion disks – binaries:general – galaxies:nuclei

## 1. Introduction

There is growing evidence that most galaxies have the supermassive black holes at their centers (Kormendy & Richstone 1995; see also Rees 1984 for a classical review). The remarkable evidence for supermassive black holes is provided by the existence of a gas disk with Keplerian rotation on a subparsec scale found by the radio observations (Miyoshi et al. 1995) and by the asymmetric iron line profile discovered by the X-ray observations (Tanaka et al. 1995). In the vicinity of a supermassive black hole, the gas in the disk is heated up and produces very high luminosity by efficiently transforming their gravitational energy into radiation (e.g., Lynden-Bell 1969) Thus, such rotating gas disks with accretion flow are considered as the energy sources of active galactic nuclei (AGNs) and quasars.

Recently, it has been widely accepted that the supermassive black holes play an important role not only in activities of AGNs and quasars, but also in the formation and global evolution of galaxies (Silk & Rees 1998; Kaufmann & Haehnelt 2000; Di Matteo et al. 2005;

Merritt 2006, and references therein). The discovery of the tight correlation between black hole mass and the velocity dispersion of the bulge component of galaxies (Ferrarese & Merritt 2000; Gebhardt et al. 2000) supports the scenario that the black holes have grown in mass through the hierarchical galaxy mergers, just as galaxies themselves. If this scenario is correct, supermassive binary black holes (BBHs) will be inevitably formed during the course of galaxy mergers (Milosavljević & Merritt 2001).

There are actually a number of observational indications that some galaxies harbour supermassive BBHs at their centers. Main results are listed as follows (see also Komossa 2003; 2006);

- Periodic optical and radio outbursts (e.g., OJ287) (Sillanpää et al. 1988; Lehto & Valtonen 1996; Valtaoja et al. 2000; Valtonen et al. 2006).
- Wiggled patterns of the radio jet indicating precessional motions on a parsec scale (Roos et al. 1993 ; Britzen et al. 2001; Abraham & Carrara 1998; Lobanov & Roland 2005).

- X-shaped morphology of radio lobes (Merritt & Ekers 2002).
- Double compact cores with the flat radio spectrum (Maness et al. 2004; Rodriguez et al. 2006).
- Orbital motion of the compact core (Sudou et al. 2003).

It is believed that the supermassive BBHs mainly evolves via three stages (Begelman et al. 1980; Yu 2002). Firstly, each of black holes sinks independently towards the center of the common gravitational potential due to the dynamical friction with neighboring stars. When the separation between two black holes becomes as short as 1 pc or so, angular momentum loss by the dynamical friction slows down due to the loss-cone effect and a supermassive hard binary is formed. This is the second stage. Finally, the semi-major axis of the binary decreases to less than 0.01 pc at which gravitational radiation dominates, and then a pair of black holes merge into a single supermassive black hole.

If there is the gas orbiting around the supermassive BBHs during transition from the second evolutionary stage to the final evolutionary stage, one will be able to observe a signal arising from the interaction between the binary and its surrounding gas (i.e. a circumbinary disk). This disk-binary interaction could be also the predominant candidate to resolve the loss-cone problem (Armitage & Natarajan 2002; 2005; see also Artymowicz 1998). An orbital angular momentum of supermassive BBHs is transferred to the circumbinary disk, by which the gas around supermassive BBHs will be swept away. In addition, we expect that the mass inflow will take place from circumbinary disk to the supermassive BBHs, leading to the formation of accretion disks around each of black holes (i.e. circumblack-hole disks). A final configuration could be three-disk systems; one circumbinary disk and two circumblack-hole disks (see Fig. 1 for a schematic view of supermassive BBHs).

Such three-disk systems have been also seen in the context of binary star formation, where the binary is composed of young stars. Artymowicz & Lubow (1996a) found that the material infalls from circumbinary disk to the central binary through the gap and that its accretion rate modulates with the orbital phase due to an orbital eccentricity. Since then, this field has been extensively studied by Artymowicz & Lubow (1996b); Lubow & Artymowicz (1996); Bate & Bonnell (1997); Lubow & Artymowicz (2000); Günther & Kley (2002); Günther & Kley (2004); Ochi et al. (2005). Basic processes involved with the disk-binary interaction have revealed through these researches. Despite its significance, however, there is poorly known how the material accretes onto supermassive BBHs from the circumbinary disk under realistic situations. Artymowicz & Lubow (1996a) only discussed briefly the quasi-periodic behavior of optical/infrared outbursts in a blazar OJ287, in terms of the strong phase-dependent accretion onto supermassive BBHs (see also Artymowicz 1998).

In this paper, therefore, we elucidate the theory of

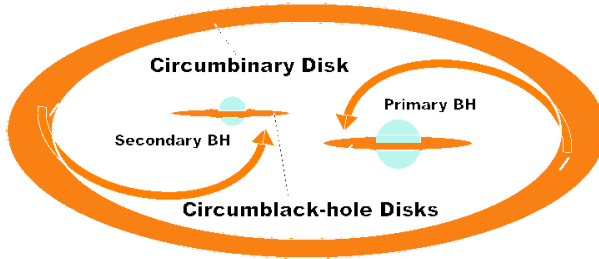


**Fig. 1.** Schematic diagram of supermassive binary black holes on a parsec/subparsec scale of merged galactic nuclei. The supermassive binary black holes are surrounded by a circumbinary disk, from which the gas overflows on to the binary, and then the circumblack-hole disks are formed around each black hole (BH).

accretion processes in supermassive binary black-hole systems, performing smoothed particle hydrodynamics (SPH) simulations. Our ultimate goal is to give an observable diagnosis for the presence of supermassive BBHs in central region of merged galaxies. The simulation should ideally take account of all the processes at work in the three-disk systems, including the circumbinary disk evolution around the supermassive BBHs, the mass transfer from the circumbinary disk to the individual black holes, and the accretion onto the each of black holes. Such a simulation, however, would require an enormous computational time. Therefore, we confine ourselves to simulate only the accretion flow from the circumbinary disk onto the supermassive BBHs. Detailed structure and evolution of the circumblack-hole disks will be reported in a subsequent paper.

The plan of this paper is as follows: We first describe our numerical model in Section 2. Then, our numerical results will be reported in Section 3 for the basic processes involved with mass accretion onto the circular, equal-mass binary, and in Section 4 for the effects of the orbital eccentricity and the unequal masses of the binary. We discuss the observational implications and the related issues in Section 5. Section 6 is devoted to conclusions.

## 2. Our Models, Basic Equations, and Numerical Procedures

### 2.1. Basic Equations

Simulations presented here were performed with a three-dimensional (3D) SPH code. The SPH code is basically the same as that used by Hayasaki & Okazaki (2004; 2005; 2006), and is based on a version originally developed by Benz (Benz 1990; Benz et al. 1990). The SPH equation with the standard cubic-spline kernel are integrated using a second-order Runge-Kutta-Fehlberg integrator with individual time steps for each particle (Bate et al. 1995), which results in an enormous computational saving when a large range of dynamical timescales are involved. We first give the basic equations and then describe the implementations to the SPH code.

### 2.1.1. Mass Conservation

In the SPH calculations, each particle has a density distribution over a spatial scale of the smoothing length,  $h$ , around its center. Hence, the density at the position of particle  $i$  ( $i = 1, 2, \dots$ ) is given by a weighted summation over the masses of the particle  $i$  itself and its neighboring particles (hereafter, neighbors),

$$\rho_i = \sum_j^{N_{\text{nei}}} m_j W(r_{ij}, h_{ij}). \quad (1)$$

Here  $m_j$  is the mass of the particle  $j$ ,  $N_{\text{nei}}$  is the number of the neighbors of the particle  $i$ ,  $r_{ij} = |\mathbf{r}_i - \mathbf{r}_j|$  is the distance between the particles  $i$  and  $j$ ,  $h_{ij} = (h_i + h_j)/2$  is the mean smoothing length, and  $W$  is the kernel. We adopt the standard cubic-spline kernel  $W$  for 3D; that is,

$$W(r, h) = \frac{1}{\pi h^3} \begin{cases} 1 - \frac{3}{2}s^2 + \frac{3}{4}s^3 & \text{if } 0 \leq s < 1, \\ \frac{1}{4}(2-s)^3 & \text{if } 1 \leq s < 2, \\ 0 & \text{otherwise,} \end{cases} \quad (2)$$

where  $s \equiv |r_{ij}/h_{ij}|$ . The mass conservation is thus automatically satisfied.

### 2.1.2. Momentum Equation

The momentum equation for the fluid under a gravity in the inertia frame is written by

$$\frac{d\mathbf{v}}{dt} = -\frac{\nabla P}{\rho} - \frac{\mathbf{F}_{\text{vis}}}{\rho} - \nabla \phi, \quad (3)$$

where  $d/dt$  is the Lagrangian derivative,  $\mathbf{v}$  is the velocity field,  $P$  is the pressure,  $\mathbf{F}_{\text{vis}}$  is the viscous force, and  $\phi$  is the gravitational potential by the BBHs. Self-gravity of the gas particles is neglected. The corresponding SPH momentum equation for the  $i$ -th particle in the potential of a pair of black holes is then

$$\frac{d\mathbf{v}_i}{dt} = -\sum_j^{N_{\text{nei}}} m_j \left( \frac{P_i}{\rho_i^2} + \frac{P_j}{\rho_j^2} + \Pi_{ij} \right) \nabla_i W(r_{ij}, h_{ij}) - \frac{GM_p(\mathbf{r}_i - \mathbf{R}_p)}{|\mathbf{r}_i - \mathbf{R}_p|^3} - \frac{GM_s(\mathbf{r}_i - \mathbf{R}_s)}{|\mathbf{r}_i - \mathbf{R}_s|^3} \quad (4)$$

where  $v_i$  is the velocity of the  $i$ -th particle,  $G$  is the gravitational constant,  $M_p$  and  $M_s$  are the masses of the primary and secondary black holes, respectively,  $\mathbf{R}_p$  and  $\mathbf{R}_s$  are the position vectors of the primary and secondary black holes, respectively, and  $\Pi_{ij}$  is the SPH artificial viscosity with the following standard form (Monaghan & Gingold 1983),

$$\Pi_{ij} = \begin{cases} (-\alpha_{\text{SPH}} c_s \mu_{ij} + \beta_{\text{SPH}} \mu_{ij}^2) / \rho_{ij} & \mathbf{v}_{ij} \cdot \mathbf{r}_{ij} \leq 0 \\ 0 & \mathbf{v}_{ij} \cdot \mathbf{r}_{ij} > 0, \end{cases} \quad (5)$$

where  $\alpha_{\text{SPH}}$  and  $\beta_{\text{SPH}}$  are the linear and non-linear artificial viscosity parameters, respectively.  $\rho_{ij} = (\rho_i + \rho_j)/2$ ,  $\mathbf{v}_{ij} = \mathbf{v}_i - \mathbf{v}_j$  and  $\mu_{ij} = h_{ij} \mathbf{v}_{ij} \cdot \mathbf{r}_{ij} / (r_{ij} + \eta_{ij})$  with  $\eta_{ij}^2 = 0.01 h_{ij}^2$ . The connection with the disk viscosity will be described in subsection 2.2.3.

### 2.1.3. Equation of State

The pressure term  $P$  in the momentum equation is calculated by the isothermal equation of state;

$$P_i = c_s^2 \rho_i, \quad (6)$$

where  $c_s$  is the isothermal sound speed of the gas. We do not need to explicitly solve an energy equation.

### 2.2. Disk Viscosity

Viscosity is essential in the disk simulations, while the SPH formalism already contains the artificial viscosity. There is an approximate relation connecting the Shakura-Sunyaev viscosity parameter  $\alpha_{\text{SS}}$  and the SPH artificial viscosity parameter  $\alpha_{\text{SPH}}$ . The outline of formalism is presented below in the same procedure as that of Section 2.1 of Okazaki et al. (2002).

Meglicki, Wickramansige & Bicknell (1993) found that the SPH viscous force becomes

$$\mathbf{F}_{\text{vis}} = \frac{1}{10} \alpha_{\text{SPH}} c_s h [\nabla^2 \mathbf{v} + 2 \nabla (\nabla \cdot \mathbf{v})] \quad (7)$$

in the 3D continuum limit of equation (5), assuming that the density varies on a length-scale much longer than that of the velocity. This implies that the shear viscosity  $\nu$  and the bulk viscosity  $\nu_{\text{bulk}}$  are given by

$$\nu = \frac{1}{10} \alpha_{\text{SPH}} c_s h \quad (8)$$

and

$$\nu_{\text{bulk}} = \frac{5}{3} \nu, \quad (9)$$

respectively.

According to the  $\alpha$  viscosity prescription (Shakura & Sunyaev 1973), on the other hand, the shear viscosity is written as

$$\nu = \alpha_{\text{SS}} c_s H, \quad (10)$$

where  $H$  is the disk scale-height and  $\alpha_{\text{SS}}$  is the viscosity parameter. From the combinations of equations (8) and (10), we find the relation connecting  $\alpha_{\text{SPH}}$  and  $\alpha_{\text{SS}}$  as

$$\alpha_{\text{SS}} = \frac{1}{10} \alpha_{\text{SPH}} \frac{h}{H}, \quad (11)$$

as long as  $\nabla \cdot \mathbf{v} = 0$  holds. However, we usually find  $\nabla \cdot \mathbf{v} \neq 0$  in general flows. Moreover, the viscosity is artificially tuned off for divergent flows in our model (see equation 5). Therefore, equation (11) should be taken as a rough approximation to relate  $\alpha_{\text{SPH}}$  to  $\alpha_{\text{SS}}$ . We adopt a constant value of  $\alpha_{\text{SS}} = 0.1$  throughout the simulations. Hence,  $\alpha_{\text{SPH}} = 10 \alpha_{\text{SS}} H/h$  is variable in space and time, while  $\beta_{\text{SPH}} = 0$  everywhere.

### 2.3. Initial Settings

We put a pair of black holes on the  $x$ - $y$  plane with the semi-major axis of the binary orbit being along the  $x$ -axis initially and the center of mass being at the origin. In the case of an eccentric binary, we set a pair of black holes initially with the minimum separation (i.e., at the periastron). That is, black holes are initially at  $(x, y) = (a(1-e), 0)$  and at  $(x, y) = (-a(1-e), 0)$ , where  $a$  is the semi-major axis and  $e$  is the eccentricity. In addition, each black hole is given an appropriate initial rotation velocity so as to orbit around the origin with given  $a$  and  $e$ . In the

present study, we fix  $a = 0.1\text{pc}$ . As for the eccentricity, we calculate two cases;  $e = 0$ , and 0.5. The unit of time is  $P_{\text{orb}} \simeq 300\text{yr}$ , unless noted otherwise.

We assume that the black holes are both Schwarzschild black holes. The masses of the primary and the secondary black holes are  $M_p$  and  $M_s$ , respectively. The binary has the mass ratio  $q = M_s/M_p$  and the total mass  $M_{\text{tot}} \equiv M_p + M_s = 10^8 M_{\odot}$ . The black holes are modeled by sink particles with the fixed accretion radius of  $r_{\text{acc}} = 0.2a$  which are  $\sim 8.0 \times 10^3$  times as large as the Schwarzschild radius. Numerically, we take away all the particles which enter the region inside  $r_{\text{acc}}$ . To ensure that the simulation results do not depend on the accretion radius, we also performed a simulation with  $r_{\text{acc}} = 0.1a$ , finding no qualitative and quantitative differences within estimated errors of  $\sim 13\%$ .

The circumbinary disk is initially set around the common center of mass of supermassive BBHs, which is coplanar with the binary orbital plane. It has a radially random density profile over a width of  $0.05a$  and a vertically isothermal, thin disk density profile, and its initial mass is  $1.0 \times 10^{-4} M_{\odot}$ . The disk material is rotating around the origin with the Keplerian rotation velocity. The inner edge of the circumbinary disk is taken as  $r_{\text{edge}} = 1.68a$  for the circular binary and  $r_{\text{edge}} = 2.75a$  for the eccentric binary.

In the circular binary, the radius of  $r = 1.68a$  corresponds to the tidal truncation radius, where the tidal torque of the binary equals to the viscous torque of the circumbinary disk. A circumbinary disk around a circular binary is truncated at this radius (Papaloizou & Pringle 1977). The tidal truncation radii for circular binaries with non-extreme masses are distributed between  $r/a = 1.68$  and  $r/a = 1.78$ , which are given by Table 1 of Artymowicz & Lubow (1994). In the eccentric binary, on the other hand, we take the (2,1) corotation radius at  $r = 2.75a$  (see section 4.1 for the detailed explanation).

The circumbinary disk is assumed to have the temperatures of  $T = 5000\text{K}$  everywhere. Note that this temperature roughly corresponds to the typical effective temperature of a standard disk around a single black hole with  $10^8 M_{\odot}$  (Kato et al. 1998). The gas particles are added randomly at the radius of the initial outer edge of the circumbinary disk, at a constant rate,  $\dot{M}_{\text{inj}} = 1.0 M_{\odot}\text{yr}^{-1}$  in all the calculated models.

We set an outer boundary at  $r = 6.0a$ , which is sufficiently far from the disk region so that the outer boundary should not affect the mass-inflow processes. The SPH particles passing outward across the outer boundary are removed from the simulation.

#### 2.4. Simulation Implementations

In our code, the accretion flow is modeled by an ensemble of gas particles, each of which has a negligible mass chosen to be  $1.0 \times 10^{-7} M_{\odot}$  with a variable smoothing length. We have carried out several simulations with different parameters. The parameters adopted by the calculated models are summarized in Table 1.

To check if the number of SPH particles used in this

study is large enough, we also performed the same simulation but with about a half as many particles as in model 1, finding no appreciable changes. In order to see the validity of the simulations, we also checked several simulation values, such as the ratio of the smoothing length to the disk scale-height  $h/H$ , the ratio of the smoothing length to the disk radius  $h/r$ , and the relative disk scale-height  $H/r$ , respectively. Here the disk scale-height  $H$  is defined as the half thickness at which the density decreases by a factor of  $e^{-1/2}$ . We have found  $h/r \gg 1$  in the range of  $1.68a \leq r \leq 4.0a$ ; that is, the radial structure of the circumbinary disk is well resolved. We also found  $h/r \sim 0.03$  at the inner edge of the disk, which ensures the justification of the size of accretion radius,  $r_{\text{acc}} = 0.2a$ . The disk is geometrically thin because of  $H/r < 0.01$  over the whole radial region, as expected from the standard disk theory. However, the vertical structure of the disk is not resolved by our SPH simulations, since we find  $h/H > 1$ . We, hence, focus our discussion on the radial structure and the detailed explanation of vertical structure is beyond the scope of the present paper.

### 3. Circular Binary with Equal-Mass Black Holes

In this section we consider the accretion onto the circular, equal-mass binary from the circumbinary disk (model 1) for understanding the basic characteristics of the accretion flow.

#### 3.1. Overall Evolution

We first overview the global evolution of the supermassive BBH systems. Fig. 2 gives snapshots of the accretion flow in 6 evolutionary stages. These are density contours in the rotation frame co-rotating with the BBH. Both of the black holes and gas in the circumbinary disk are rotating in the anti-clockwise direction, although the former are rotating more rapidly than the latter according to the Kepler's law. A pair of the solid circles denote the accretion radii of black holes, which we set at  $r_{\text{acc}} = 0.2a$  from the center of the black holes. The dotted circle and dashed circle represent the tidal truncation radius,  $r_{\text{trunc}} = 1.68a$  (see section 2.3), and a trapping radius for material,  $r_{\text{trap}}/a = 1.19841$ , respectively. The trapping radius is defined as the distance from the center of mass to the outer Lagrange point,  $L_2$ . This is also the same as that from the center of mass to the  $L_3$  point in the case of circular binary with equal masses. This circle approximately points the loci of the maximum in the radial profile of the effective potential (e.g. Kitamura 1970). In other words, the material once flows inside this circle, it can freely fall towards either of the black holes.

Let us see the disk evolution, following each panel in Fig. 2. Although starting with a circular shape around the center of mass at  $t = 0$  [panel (a)], the disk shape begins to be elongated [see panel (b) at  $t = 0.35$ ]. Such deformation continues to grow as the time goes on, and eventually the inner edge of the circumbinary disk touches the circle of the trapping radius at two points at  $t = 0.54$  [see points P and Q in panel (c)]. Then, gas starts to flow

**Table 1.** Summary of model simulations. The first column represents the model numbers. The second column is the run time in units of  $P_{\text{orb}}$ . The mass ratio and the eccentricity are given in the third column and the fourth column, respectively. The last column is the initial radius of the inner edge of the circumbinary disk.

Model	Run time ( $P_{\text{orb}}$ )	Mass ratio $q$	Eccentricity $e$	Initial disk-inner edge $r_{\text{edge}}/a$
1	40	1.0	0.0	1.68
2	60	1.0	0.5	2.75
3	40	0.5	0.0	1.75
4	60	0.5	0.5	2.75

towards the black holes across these two points (particularly, via the point Q), being gravitationally attracted by the black holes. But this inflow is only a transient one for  $0 \leq t < 1$ . Subsequently, the gas is gradually accumulated on the two points as shown in panel (d). After  $t = 3.75$ , the gas starts to continuously overflow via points P and Q. The gas inflow will eventually form an accretion disk (i.e., circumbinary disks) around each black hole. The possibility of circumbinary disk formation will be discussed in section 3.4.

### 3.2. Why is the Disk Elongated?

Fig. 2 clearly demonstrates that the disk elongation triggers mass inflow towards the black holes. Then, what is the key physics underlying the disk deformation? To understand the physics, we performed the pressure-less particle simulation, in which we dropped all the terms related to pressure and viscosity ( $P_i = \Pi_{ij} = 0$  in equation 4), adopting the same parameters as those in model 1. The resultant evolution is very much similar to those we obtained in model 1, including the angle of the elongation, in the initial evolutionary stage for  $0 < t < 1$ . This examination unambiguously proves that the key physics causing the disk elongation should be of kinematics; that is, the tidal interaction between the circumbinary disk and the BBHs is responsible. Note that the resonance interaction between the disk and the binary will be effective after several orbital periods (e.g. Artymowicz & Lubow 1994).

Why is, then, the semi-major axis of the elongated disk misaligned with the line connecting the primary and the secondary black holes as seen in panel (b) of Fig. 2? This phase shift mechanism seems to be due to the tidal friction, that is, the same mechanism as what causes the phase shift of the tidal bulge in the earth-moon system (MacDonald 1964). This phase shift mechanism is well understood by using the forced harmonic oscillator model (see Murray & Dermott 1999). The general solution of the forced harmonic oscillator becomes  $A \cos(\omega t + \delta)$ , where  $A$  is the amplitude,  $\omega$  is the frequency of the external driven force and  $\delta$  just shows the phase shift, which can be written as a function of the  $\omega$  and the natural frequency and the damping time-scale. By analogy with this forced harmonic oscillator model, we interpret that the misalignment is due to the tidal friction induced by the difference between the binary frequency and the frequency of the disk-inner edge. After the disk starts to

be elongated, the disk material is accumulated in the two points on the semi-minor axis of the circumbinary disk by the gravity force of black holes. A pair of bumps (i.e., the tidal bulges) are, then, formed at the disk inner edge, as shown in panel (c) of Fig. 2.

Next, let us examine the radial structure of the circumbinary disk. The left panel of Fig. 3 shows the radial distributions of the surface density and radial velocity at  $t = 39.5$  in model 1. The solid line, the dashed line and the dash-dotted line show the surface density (in units of  $\text{g cm}^{-2}$ ), the radial velocity normalized by the free-fall velocity, and the tidal truncation radius,  $r_{\text{trunc}} = 1.68a$ , respectively. A positive (or negative) radial velocity indicates an outward (inward) flow. Clearly, the radial motion of the gas in the circumbinary disk is mostly outward, whereas it is inward inside the tidal truncation radius. Note that the upwardly convex shape of the surface density distribution may be due to an artifact of our way of mass injection (recall that we inject mass to the radius of  $r_{\text{inj}} = 1.73a$ ). However, it is unlikely that our treatment will seriously influence the mass inflow rate at the disk inner edge, since the circumbinary disk evolves on much longer timescale than the orbital period.

### 3.3. Mass Supply and Mass Capture

Let us next see long-term evolution of the mass supply from the circumbinary disk and the mass capture by the black holes. Fig. 4 illustrates the initial evolution of the mass-supply rate (upper) and the capture rates with (lower), together with that of the circumbinary disk mass (upper) and of total mass captured by black holes (lower), during  $0 \leq t \leq 20$  in model 1. The mass-capture rate is defined by how much the material is captured by each black hole at the accretion radius  $r_{\text{acc}} = 0.2a$  in units of  $\text{M}_{\odot} \text{ yr}^{-1}$ . The solid line, the dashed line and the dash-dotted line show the mass-capture rates by the primary black hole and by the secondary black hole, and the disk mass, respectively. We see in this figure that the disk mass steadily increases until  $t = 15$  and then stays nearly constant afterwards. Both mass-capture rates by the black holes also increase until  $t = 15$  and saturate afterwards but show substantial fluctuations. We can thus safely conclude that mass supply and accretion flow reach their quasi-steady state after  $t \simeq 15$ .

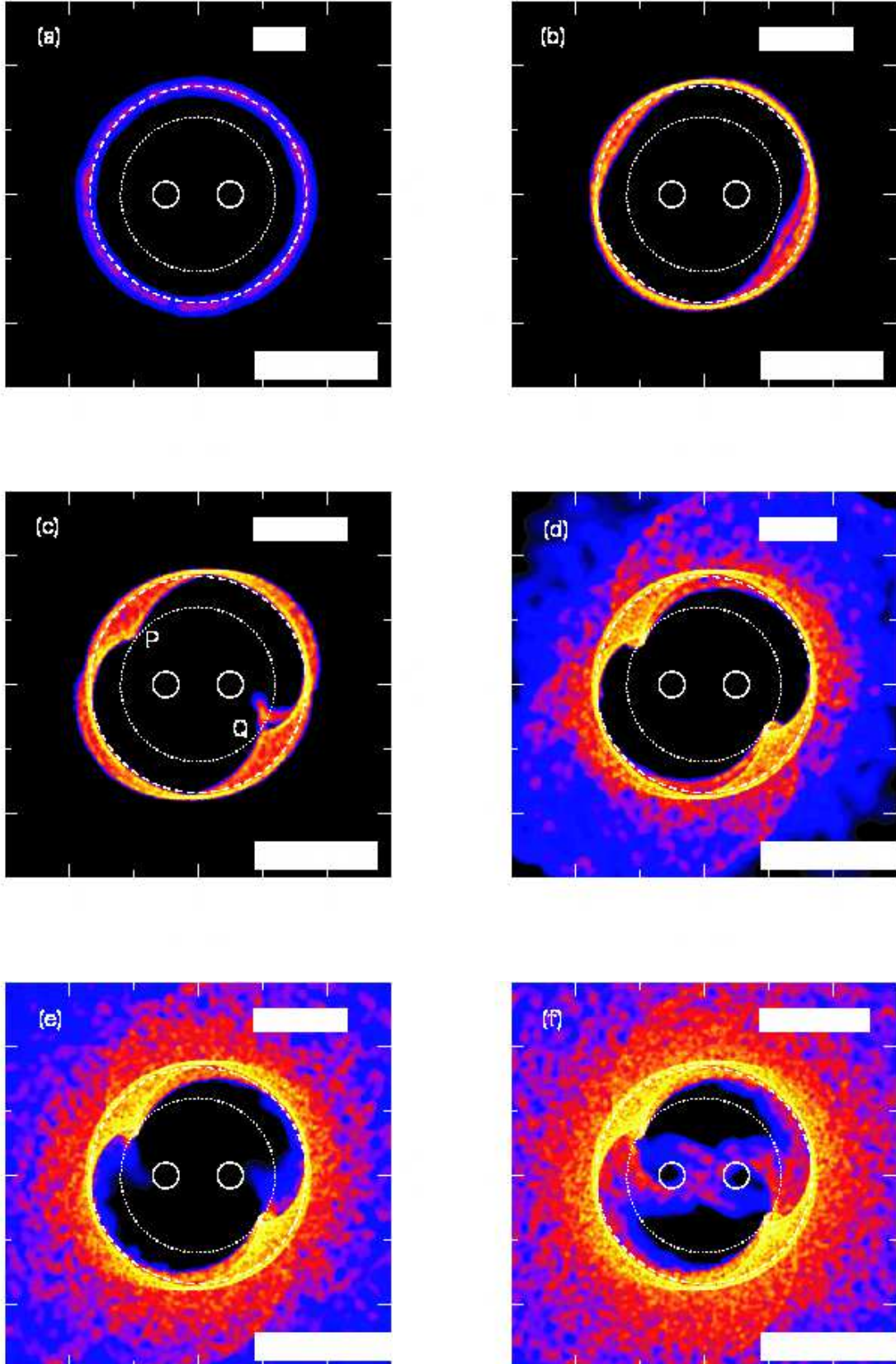


**Fig. 2.** Snapshots of accretion flow from the circumbinary disk onto the supermassive BBHs in model 1. The origin is set on the center of mass of the binary and all panels are shown in a binary rotation frame. Each panel shows the surface density in a range of three orders of magnitude in the logarithmic scale. The solid circle denotes the accretion radius of the primary black hole and the secondary black hole, respectively. The dashed and dotted circle represents the tidal truncation radius and the outer Roche-lobe radius of  $q = 1.0$  along with  $L_2$  and  $L_3$ , respectively. Annotated in each panel are the time in units of  $P_{\text{orb}}$  and the number of SPH particles  $N_{\text{SPH}}$ .

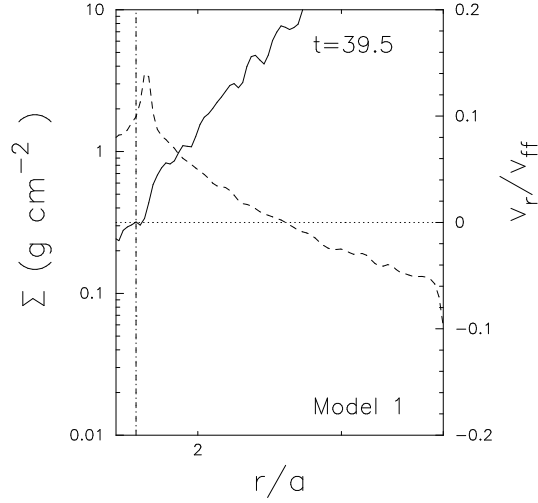


**Fig. 3.** Radial distributions of the surface density (dashed line) and radial velocity (solid line) normalized by the free-fall velocity at  $t = 39.5$  in model 1. The dash-dotted line indicates the position of the tidal truncation radius  $r_{\text{trunc}} = 1.68a$ . A positive (or negative) radial velocity means the outward (inward) flow.

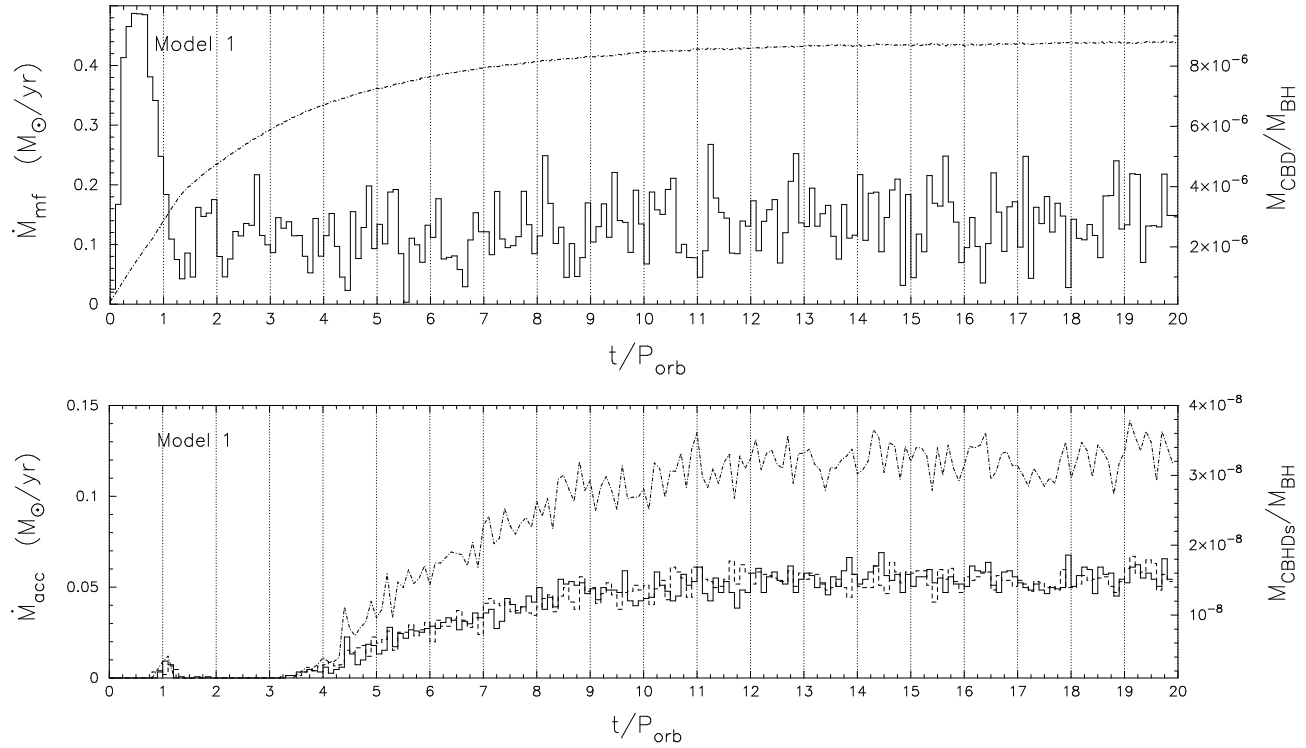


**Fig. 4.** Evolution of the azimuthally averaged mass flux  $\dot{M}_{\text{mf}}$  at the tidal truncation radius  $r_{\text{trunc}} = 1.68a$  and the mass of circumbinary disk  $M_{\text{CBHD}}$  (upper panel), and of the mass-capture rate  $\dot{M}_{\text{acc}}$  and the total mass captured by black holes  $M_{\text{CBHDs}}$  (lower panel) in model 1. In the upper panel, the solid line and the dash-dotted line denote the azimuthally averaged mass flux and the mass of the circumbinary disk normalized by total black-hole mass  $M_{\text{BH}}$ , respectively. In the lower panel, the solid line, the dashed line and the dash-dotted line show the mass capture rate of the primary black hole, that of the secondary black hole and the total mass captured by black holes in units of  $M_{\text{BH}}$ , respectively.

### 3.4. Circumblack-hole Disk Formation

Hayasaki & Okazaki (2004) discussed the possibility of the accretion disk formation around the neutron star in a Be/X-ray binary using the data of SPH particles captured by the neutron star. In this subsection, we discuss a possibility of the circumblack-hole disk formation around each black hole in model 1, adopting a similar approach as that in section 2.3 of (Hayasaki & Okazaki 2004).

The material captured at  $r_{\text{acc}}$  has a specific angular momentum  $J$ , by which we can infer the circularization radius of the gas particles,  $R_{\text{circ}} = J_i^2/GM_i$ , where suffix  $i=p$  refers to the primary black hole and  $i=s$  to the secondary one. The upper panel of Fig 5 shows the orbital dependence of the circularization radius, where the solid line and the dashed line denote the circularization radius of the primary and the secondary, respectively. This figure clearly shows that the circularization radii largely exceed the Schwarzschild radii of the black holes. Thus, the formation of a disk around each black hole is very likely.

The lower panel of Fig 5 denotes the viscous timescale of each circumblack-hole disk evaluated at  $R_{\text{circ}}$ . For simplicity, we assume the circumblack-hole disk to be geometrically thin and isothermal with the Shakura-Sunyaev viscosity parameter  $\alpha_{\text{SS}}$ . The ratios of  $\tau_{\text{vis}}/P_{\text{orb}}$  for the primary and the secondary black holes are given, respectively, by

$$\frac{\tau_{\text{vis}}}{P_{\text{orb}}}\Big|_p = \frac{1}{2\pi\alpha_{\text{SS}}c_s^2} \left(\frac{R_{\text{circ}}}{a}\right)^{1/2} \frac{GM_p}{a} (1+q)^{1/2}, \quad (12)$$

$$\frac{\tau_{\text{vis}}}{P_{\text{orb}}}\Big|_s = \frac{1}{2\pi\alpha_{\text{SS}}c_s^2} \left(\frac{R_{\text{circ}}}{a}\right)^{1/2} \frac{GM_s}{a} \left(1 + \frac{1}{q}\right)^{1/2}. \quad (13)$$

The orbital phase dependence of  $\tau_{\text{vis}}/P_{\text{orb}}$  is shown in the lower panel of Fig 5. It is immediately seen that the viscous timescales in each of circumblack-holes disks are much longer than the orbital period.

## 4. Effects of Eccentricity and Unequal Masses

In this section, we first discuss the effects of an orbital eccentricity, which gives rise to interesting orbital-phase modulations. We then touch on the cases with unequal mass black holes.

### 4.1. Eccentric Binary with Equal-Mass Black Holes

The evolution of supermassive BBHs with an orbital eccentricity has been discussed extensively (e.g. Roos 1981 ; Polnarev & Rees 1994; Rauch & Tremaine 1996; Quinlan & Hernquist 1997 ; Armitage & Natarajan 2005). The eccentricity could grow secularly due to the interaction between the black hole and its ambient stellar medium, although this feature has not yet obtained general consensus. In this section, we describe the accretion flow from the circumbinary disk onto the central binary with an eccentricity  $e = 0.5$ .

Fig.6 shows snapshots of accretion flow around supermassive BBHs with eccentricity  $e = 0.5$  and equal masses  $q = 1.0$ . Here, the dotted circle and the dashed circle

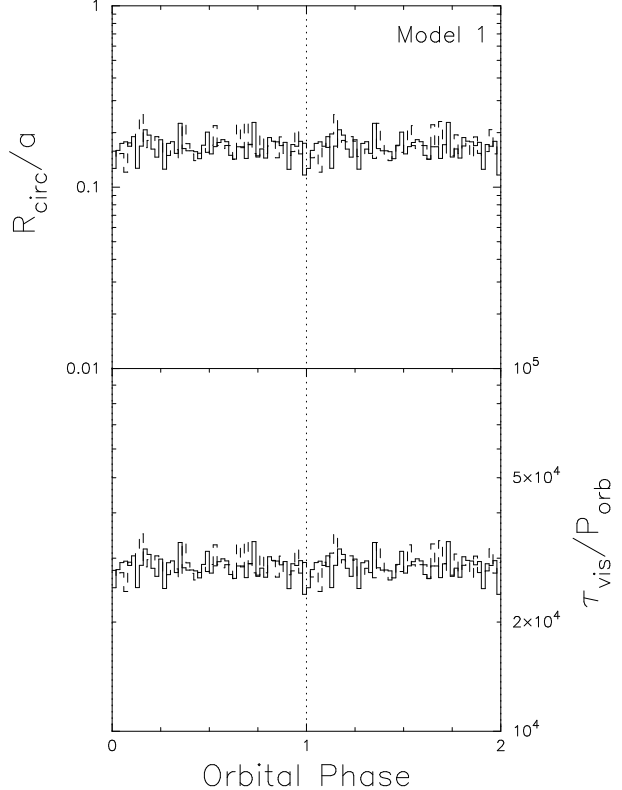


**Fig. 5.** Orbital phase dependence of the circularization radius (upper panel) and the ratio of the viscous-time scale to the orbital period (lower panel) for the primary (solid lines) and the secondary (dotted lines) black hole, respectively in model 1.

correspond to the radius of the (2, 1) corotation resonance and that of the (2, 1) outer Lindblad resonance, respectively, where the  $(m, l)$  corotation resonance radius and the  $(m, l)$  outer Lindblad resonance radius are given, respectively, by  $(m/l)^{2/3}a$  and  $((m+1)/l)^{2/3}a$  for a circumbinary disk. Here  $m$  and  $l$  are the azimuthal and time-harmonic numbers, respectively, in a double Fourier decomposition of the binary potential,  $\Phi(r, \theta, t) = \sum \phi_{m,l}(r) \exp[i(m\theta - l\Omega_B t)]$ , where  $\Omega_B$  is the orbital frequency of the binary (Artymowicz & Lubow 1994).

After the disk is set up (see panel (a) of Fig. 6), the tidal bulge is formed and the gas reaches the radius of the (2,1) outer Lindblad resonance at  $t = 1.5$ , as is seen in panel (b) of Fig 6. The semi-major axis of the elongated disk is not aligned with that of the binary as well as in a circular binary (see panel (b) of Fig. 2). This phase shift of the tidal bulge occurs by the tidal friction, as in the case of circular binaries. The unique feature seen in the case of eccentric binaries is that since the binary separation is periodically changing with time, the phase shift should also be changing with time. In addition, the gravitational attraction force also changes periodically and is maximum for the closest parts of the disk to black holes at the phase of the maximum binary separation (i.e., at the apastron).

The material around the binary will be swept away, since it acquires angular momentum transferred from the

BBHs. This transfer is induced by the resonance interaction between the binary and the circumbinary disk (see Artymowicz & Lubow 1994; 1996a; 1996b; Lubow & Artymowicz 1996; 2000). As a result, the inner edge of the circumbinary disk is truncated roughly at the (2,1) outer Lindblad resonance as seen in panels (c)-(f) of Fig 6.

#### 4.2. Gap Opening and Closing

Panels (c)-(f) of Fig 6 represent sequential snapshots of accretion flows in this system for  $39 < t < 40$ . While the material inside the (2,1) corotation radius is captured by the black holes, the mass outside the (2,1) corotation radius outwardly flows at  $t = 39.02$ . Subsequently, most of the material is swallowed by black holes at  $t = 39.25$ , whereas the gas keeps the outward flow outside the (2,1) corotation radius. The mass overflow is, then, initiated at  $t = 39.5$ , and the gas falls and reaches the BBHs at  $t = 39.79$ . The most conspicuous feature in the evolution of model 2 resides in this periodic on/off transitions of mass supply. In the absence of the mass inflow from the circumbinary disk a big gap appears between the disk and the black holes. We call this the gap-opening phase. When the mass inflow occurs from the circumbinary disk and then make bridges from the disk to the BBHs, the gap is closed. This is the gap-closing phase. The typical four stages in one gap-closing and opening cycle is repeated in sequential order. In contrast, there is a continuous mass supply to the black holes (i.e., the gap is always closed) in model 1.

As seen in panel (c) of Fig. 6, the circumbinary disk stops mass inflow towards its inner edge when the binary is at the periastron (phase 0), whereas the mass which already left the (2,1) corotation radius continues to fall on to each black hole by the gravitational attraction. Here, Fig. 7 displays the radial distributions of the surface density and the radial velocity in the circumbinary disks in the two different phases. The left panel shows that the radial velocity is almost everywhere outward at phase 0.25, meaning no mass inflow, whereas there is mass inflow at the apastron (phase 0.5).

We need to distinguish the following two steps to understand the orbital modulation of the mass flow stream: (1) When the binary is at the periastron, the angular momentum is much more transferred from the binary to the circumbinary disk than otherwise. Accordingly, the gas inflow is terminated after the periastron [see panel (c)]. Conversely, the mass inflow is at maximum around the apastron. (2) the material which was launched from the circumbinary disk at the apastron will take some time to reach the BBHs. Hence, there arises a phase-lag between the mass-supply maximum and the mass capture maximum, which roughly corresponds to the free-fall time from the circumbinary disk to the black holes. As a result, the majority of infalling gas is captured by the black holes just before the periastron [see panel (f)]. Hence, the gap starts to be closed after the apastron and is completely closed before the periastron (at phase  $\sim 0.75$ ), and then is opened again after the periastron (at phase  $\sim 0.25$ ).

#### 4.3. Mass Supply and Mass Capture

Owing to the reason mentioned above, there arises a phase delay between the moment of the maximum azimuthally-averaged mass flux and that of the maximum mass-capture rate. We next show how the mass-capture rate and the averaged mass flux vary with binary orbital motion. The upper panels of Fig. 8 depict the azimuthally averaged mass flux and the mass-capture rate. To reduce the fluctuation noise, these data are folded on the orbital period over  $40 \leq t \leq 60$  after the system is the quasi-steady state ( $t \geq 38$ ).

The left-lower panel of Fig. 8 shows the azimuthally averaged mass flux at the (2,1) corotation radius in model 2. While the circumbinary disk has an outward flow from the periastron passage to the phase somehow before apastron, the mass is inwardly launched from the disk-inner edge from the phase somehow before apastron to the next periastron. This also supports that the gap is opening after the periastron and the gap is closing after the apastron in the eccentric binary.

The right-lower panel of Fig 8 represents the orbital-phase dependence of the mass-capture rate and the corresponding luminosity normalized Eddington luminosity with total black hole mass  $10^8 M_\odot$ ; i.e.,  $L_E \sim 10^{46}$  erg s $^{-1}$ , in model 2. Despite the fact that we continuously inject mass to the circumbinary disk at a rate of  $\dot{M}_{\text{inj}} = 1.0 M_\odot \text{yr}^{-1}$ , which would produce about the Eddington luminosity for  $\eta \sim 0.1$ , the calculated luminosity is substantially sub-Eddington. This is because the majority of the injected mass is lost in this system. The solid line and dashed line denote the mass-capture rate by the primary black hole and by the secondary one, respectively. This figure clearly shows that the mass-capture rate significantly modulates with the orbital motion. The peak of mass-capture rate is located in before the periastron passage. Furthermore, the ratio of the lowest mass-capture rate to the highest one during one orbital period is  $\sim 1/10$ .

For comparison, we give the same but for model 1 in the upper panels of Fig. 8. This figure clearly represents that the circumbinary disk continues to supply the gas to its inner regions over the whole orbital period. Then, the gas falls onto each black hole with fluctuations. This behavior is mainly caused by the overflow as seen in the last two panels of Fig 2.

#### 4.4. Unequal Masses

Finally, we discuss the cases of unequal mass black holes. The most common binaries are likely to possess black holes with extreme mass ratios in the case of the minor galactic mergers (Armitage & Natarajan 2002; Armitage & Natarajan 2005). If the binaries are formed as a result of a major merger, on the contrary, its mass ratio can be non-extreme and slightly deviate from unity. The effects of non-extreme but unequal masses on the accretion flow onto the supermassive BBHs are investigated by models 3 and 4 and are remarkably represented by the azimuthally averaged mass flux and the mass-capture rate by each black hole in Fig.9.

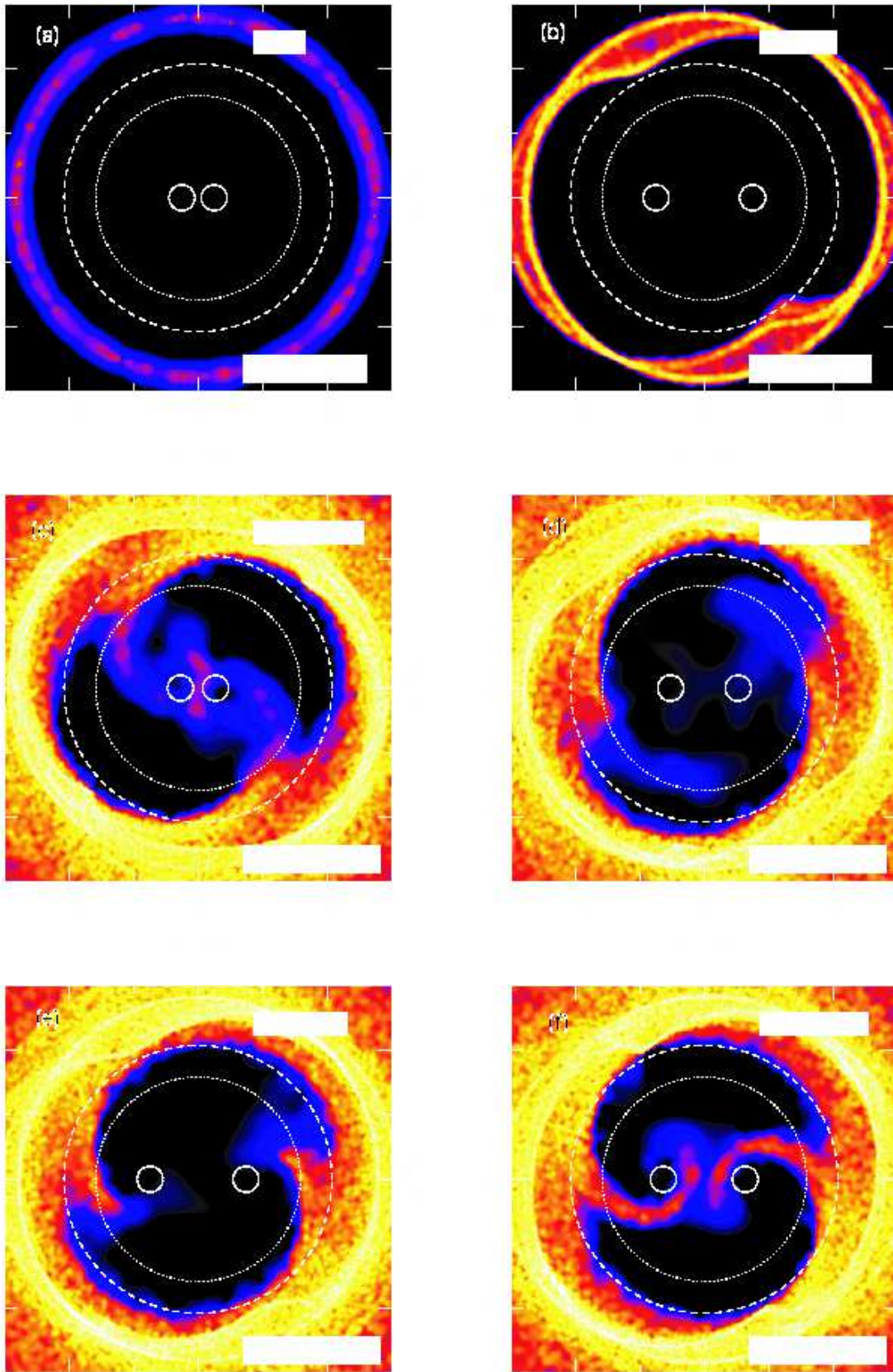


**Fig. 6.** Same formats as model 1 (Fig. 2), but for model 2. The dashed circle and the dotted circle denote the (2,1) outer Lindblad resonance radius and the (2,1) corotation radius, respectively.

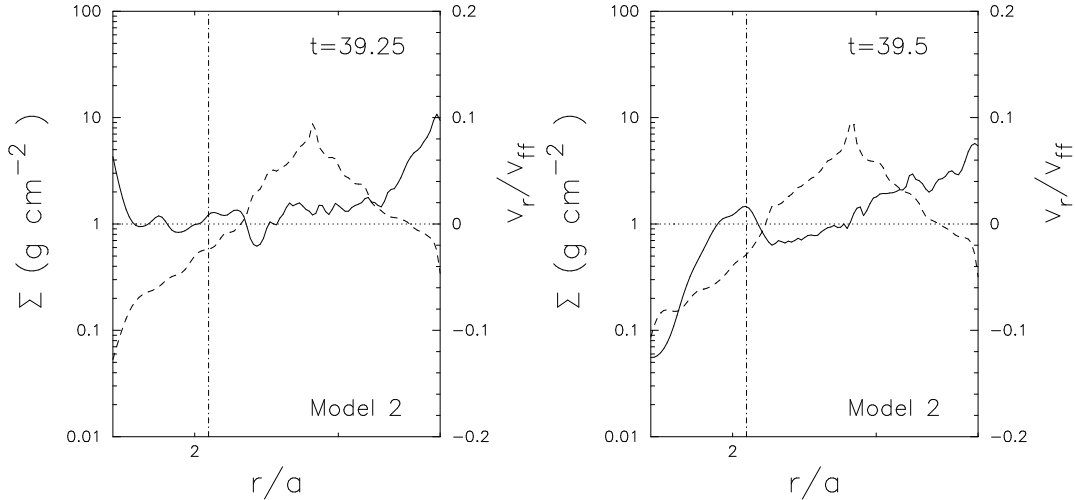


**Fig. 7.** Same format as model 1 (the left panel of Fig. 3), but for model 2. The results are shown at two different phases: at phase 0.25 and 0.5 in the left and the right panels, respectively. The dash-dotted line shows the (2,1) outer Lindblad resonance radius.

Model 3 is the run with  $(q, e) = (0.5, 0.0)$ . It is seen from the upper panels of Fig. 9 that the mass-capture rate of the secondary black hole is much higher than that of the primary one although the total mass-capture rate by both of black holes roughly equals to the azimuthally averaged mass flux. This is because the distance between the inner edge of the circumbinary disk and the  $L_2$  point is shorter than that between the disk inner edge and  $L_3$  point. Thus, the gas prefers to be attracted from the secondary black hole closer to the  $L_2$  point than the primary one.

In model 4, which is run with  $(q, e) = (0.5, 0.0)$ , the lower panels of Fig. 9 indicates that the rising time of the secondary burst is earlier than that of the primary burst. Thus, the mass captured by the secondary black hole during one orbital period is more than that by the primary black hole. This is consistent with the results of model 3, i.e., the gas is easy to be captured by secondary black hole.

## 5. Discussion

We have performed the SPH simulations of accretion flow around the supermassive BBHs. We find that the material overflows from the circumbinary disk via two points, freely infalls towards either of the BBHs, and is eventually captured by it. While the mass capture-rate has little orbital-phase dependence in the case of a circular binary, it exhibits significant orbital modulations in the case of an eccentric binary. In this section, we discuss the formation and evolution processes of the circumbinary disks, circumbinary disk evolution, shock formation near the circumbinary disks, and possible strategy to detect such BBH candidates exhibiting periodic light variations.

### 5.1. Circumbinary Disks

We have already discussed in section 3.4 a possibility of the formation of the circumbinary disks and estimated their viscous timescales at the circularization radii. In this

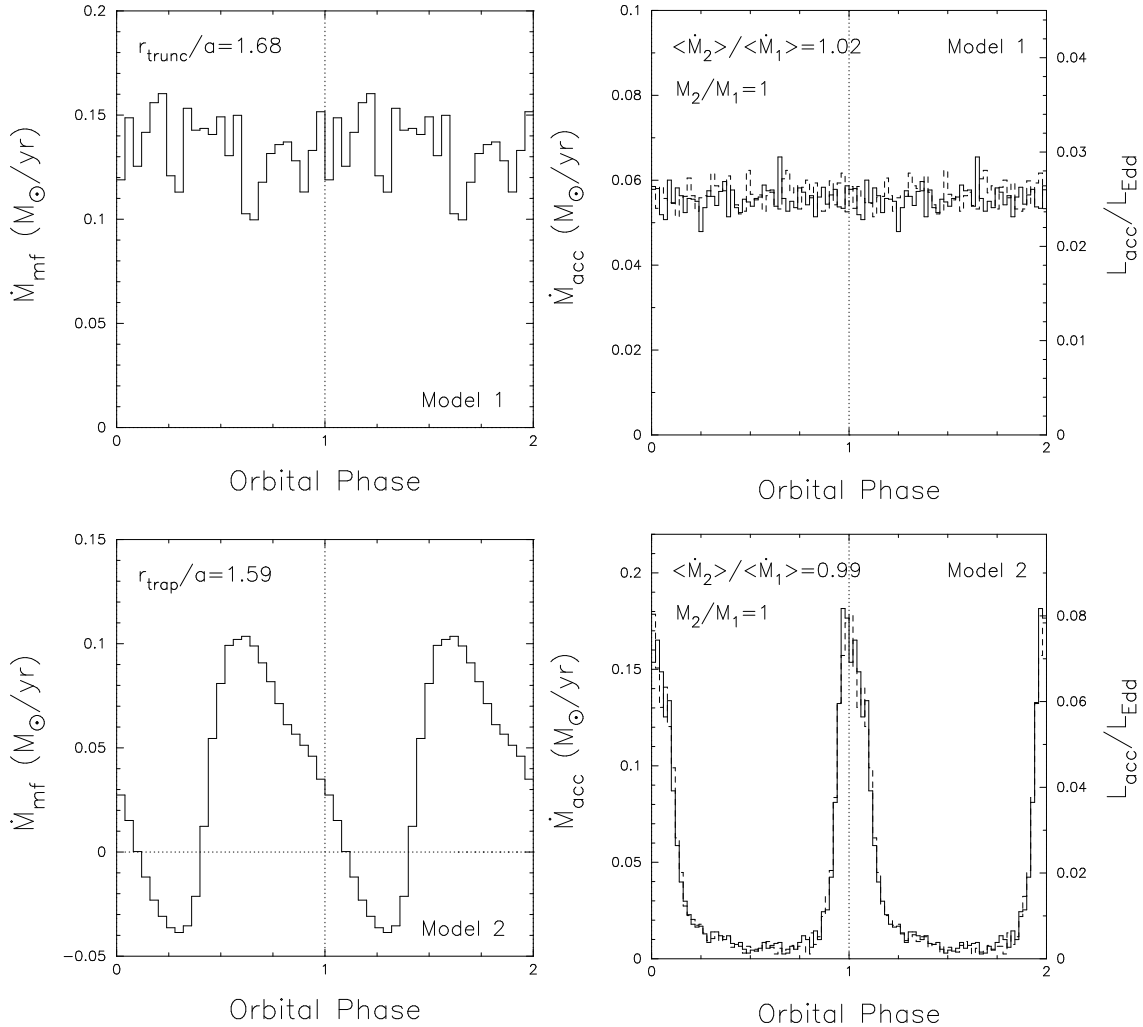
section, we discuss whether the circumbinary disks are persistent or not during one orbital period and how viscous accretion processes affect the evolution and structure of the circumbinary disk.

Table 2 summarizes the mean mass-capture rates, the mean circularization radii, and the mean viscous timescales of all the calculated models. To reduce the fluctuation noise, the simulation data are folded on the orbital period over  $20 \leq t \leq 40$  in models 1 and 3, and over  $40 \leq t \leq 60$  in models 2 and 4. The second and the third columns denote the mean mass-capture rates of the primary and the secondary black holes, respectively. These columns clearly show that the sum of the mean mass-capture rates by the BBHs in the circular binaries is higher than that of the eccentric binaries. This implies that the circumbinary disks in the circular binaries is denser than those in the eccentric binaries.

We see from the fourth column and the fifth column of Table 2, which denote the mean circularization radii around each black hole, that the size of the circumbinary disks in the circular binaries is larger than that in the eccentric binaries. In model 3, the disk size of the secondary black hole,  $R_{\text{circ},s} = 0.42a$ , is larger than the accretion radius,  $r_{\text{acc}} = 0.2a$ . This means that some of the mass which enters the sphere of  $r_{\text{acc}} = 0.2a$  may finally go out, without being captured by the black hole.

The last two columns of Table 2 represents the mean viscous time-scale of the primary black hole and of the secondary one, respectively. These are estimated by using equation 15 and 16. It is clear from these columns that the viscous time-scale is much longer than the orbital period in all the models. Thus, the once formed, the circumbinary disks will survive over the whole orbital phase. The viscosity in the circumbinary disks gives little influence on their structure and short-term evolution on the timescale of the order of the orbital period.

The phase-dependent accretion is likely to give a good impact on the outer edge of the circumbinary disk.



**Fig. 8.** Orbital-phase dependence of azimuthally averaged mass flux and mass-capture rate in models 1 (upper panels) and 2 (lower panels), respectively. The binary is at the periastron (apastron) at phase 0.0 (0.5). The data are folded on the orbital period over  $20 \leq t \leq 40$  in model 1 and over  $40 \leq t \leq 60$  in model 2. The mass flux is measured at the tidal truncation radius  $r_{trunc} = 1.68a$  in model 1 and at the (2,1) corotation resonance radius  $r_{trap} \simeq 1.59a$  in model 2, respectively. The right axis shows the X-ray luminosity corresponding to the mass-capture rate with the energy conversion efficiency,  $\eta = 0.1$ , normalized by the Eddington luminosity with total black hole mass  $M_{bh} = 1.0 \times 10^{-8} M_\odot$ , where  $\eta$  is defined by  $L_{acc} = \eta \dot{M}_{cap} c^2$ .

**Table 2.** Summary of simulation results. The first column represents model numbers. The second column is the number of SPH particles at the end of the run. The third column and the fourth column are the mean accretion rates of the primary and those of the secondary, respectively. The fifth column and the sixth column are the mean circularization radii of the primary and those of the secondary, respectively. The last two columns are the mean viscous time-scales of the primary and of the secondary, respectively. All quantities shown in the 3-8th columns are folded on the orbital period over  $20 \leq t \leq 40$  in modes 1 and 3, and  $40 \leq t \leq 60$  in models 2 and 4.

Model	$N_{SPH}$ (final)	$\langle \dot{M}_p \rangle$ ( $M_\odot \text{yr}^{-1}$ )	$\langle \dot{M}_s \rangle$ ( $M_\odot \text{yr}^{-1}$ )	$\langle R_{circ,p} \rangle$ $a$	$\langle R_{circ,s} \rangle$ $a$	$\langle t_{vis,p} \rangle$ $P_{\text{orb}}$	$\langle t_{vis,s} \rangle$ $P_{\text{orb}}$
1	64023	$5.6 \times 10^{-2}$	$5.7 \times 10^{-2}$	$1.5 \times 10^{-1}$	$1.5 \times 10^{-1}$	$2.7 \times 10^4$	$2.7 \times 10^4$
2	92633	$3.8 \times 10^{-2}$	$3.8 \times 10^{-2}$	$8.1 \times 10^{-2}$	$8.5 \times 10^{-2}$	$2.0 \times 10^4$	$2.0 \times 10^4$
3	73975	$5.5 \times 10^{-2}$	$1.8 \times 10^{-1}$	$1.0 \times 10^{-1}$	$4.2 \times 10^{-1}$	$2.6 \times 10^4$	$3.7 \times 10^4$
4	64921	$1.7 \times 10^{-2}$	$2.1 \times 10^{-2}$	$7.7 \times 10^{-2}$	$8.4 \times 10^{-2}$	$2.1 \times 10^4$	$1.6 \times 10^4$

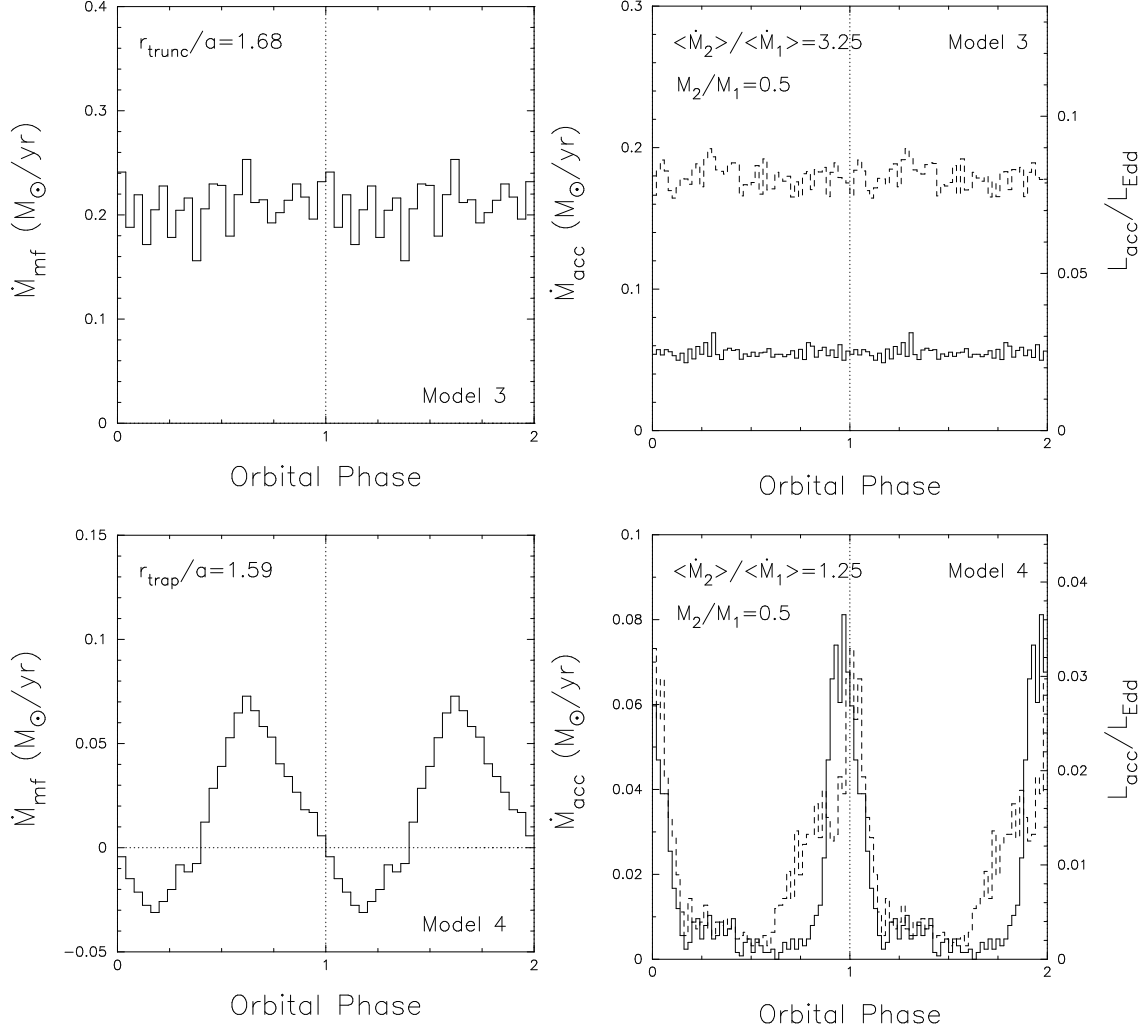


**Fig. 9.** Same formats as model 1 (Fig. 3), but for models 3 (upper panels) and 4 (lower panels), respectively.

This will be able to excite one-armed oscillations on the disk (e.g., Hayasaki & Okazaki 2005). As the one-armed waves propagates, the material on the outer region of the disk is inwardly pushed towards the central black hole. Since the propagation time-scale is roughly estimated by using  $(\alpha_{\text{SS}}/2\pi)\tau_{\text{visc}}$ , where  $\tau_{\text{visc}}$  is the viscous time-scale of circumbinary disks, as  $\sim 10^{2-3}P_{\text{orb}}$ , the outer region of the disk can significantly vary, whereas the inner region of the disk may remain to be unchanged. We thus expect that optical/IR radiation mainly from the outer portions will exhibit significant periodic variations, whereas radio and X-ray emissions coming from the innermost region may not show such periodic and coherent variations (however, see the later Section 5.3). If this is the case, the spectral energy distributions (SEDs) will be highly time-dependent on the orbital timescale.

It is likely that the mass exchanges occur via an effective L1 point between the disks around the primary and secondary black holes (e.g. Günther & Kley (2004)). In addition to the phase-dependent mass inflow from the circumbinary disk, this mass exchange could also affect the

evolution and structure of circumbinary disks. This effect cannot be, however, treated in our simulations, because of the lack of sufficient resolution to resolve the narrow region around the effective L1 point.

The right-upper (lower) panels of Fig. 8 and Fig. 9, also demonstrate that the mass-capture rate is about one-order of magnitude as low as the mass-input rate in all the models. In fact, the total mass of circumbinary disk, which approximately equals to the total mass captured by black holes  $M_{\text{CBHDs}}$ , is much lower than the mass of circumbinary disk, as shown in Fig. 4. This strongly suggests that the circumbinary disk has a significantly low density. Thus, we expect that the accretion flow should become radiatively inefficient in the vicinity of black holes (Kato et al. 1998).

### 5.2. Circumbinary Disks

We address a question; what happens if the circumbinary disk is inclined from the orbital plane of the supermassive BBHs? The mass-capture rate profile may show a two-peaked feature, because there are a couple of points

in the disk-inner edge to which the BBHs approach during one orbital period. In fact, the double-peak structure is observed in the optical outbursts of OJ287 (Stothers & Sillanpää 1997). The effect of the inclination angle on the mass-capture rate profile will be also examined in a subsequent paper.

MacFadyen & Milosavljević (2006) described the mass supply rate from the circumbinary disk mainly exhibits a quasi-periodic modulation due to the eccentricity of the circumbinary disk, even if the binary black hole has circular orbit. The disk eccentricity will be excited due to resonance interaction between the circumbinary disk and the central binary after a few viscous time-scale of the circumbinary disk. Such a longterm evolution of the circumbinary disk could also give the time variations of the light curve of circumbinary disk itself, such as a superhump phenomenon in Dwarf Novae systems (e.g., Murray 1998).

In addition, the circumbinary disk evolution could play an key role to resolve the loss-cone problem (e.g., Artymowicz 1998; MacFadyen & Milosavljević 2006). The disk-binary interaction gives an influence of the global evolution of the binary orbital elements, e.g., the eccentricity, the semi-major axis, the mass-ratio, the inclination angle and so on (Artymowicz et al. 1991; Bate & Bonnell 1997; Lubow & Artymowicz 2000). Therefore, in the framework of the disk-binary interaction, the effects of all the orbital elements should ideally be taken account of. The longterm evolution of the circumbinary disk remains as a matter to be discussed further.

### 5.3. Shock Formation

Another important issue to be considered is a possible formation of shock structure. We estimate the radial velocity at the inner boundary  $r_{\text{acc}} = 0.2a$  in model 2 and plot its orbital-phase dependence in Fig. 10. Here, the radial velocity is normalized by the free-fall velocity. We understand that the radial velocity is on the same order of magnitude of the free-fall velocity and that it suffers the orbital modulation with the peak being around the apastron (phase 0.5). This trend contrasts with that of the mass-capture rate which exhibits a peak around the periastron (see Fig. 8). If the material inflows near circumbinary disk, shock structures could be formed near the outer edge of the circumbinary disk. Substantial fraction of the kinetic energy of the material will be converted to the thermal energy. Consequently, detectable soft X-rays or UV could be periodically emitted from the shock structures. Such X-rays or UV will exhibit a broad peak around phase  $\sim 0.5$ , whereas optical/IR radiation will show a sharp peak around phase  $\sim 0.0$ .

### 5.4. Observation Implications

Sillanpää et al. (1988) firstly proposed that the periodic behavior of the optical light-curve of OJ287 may be induced by the orbital motion of the binary black holes, that is, the tidal perturbation of the secondary black hole causes the accretion rate of the primary black hole to be

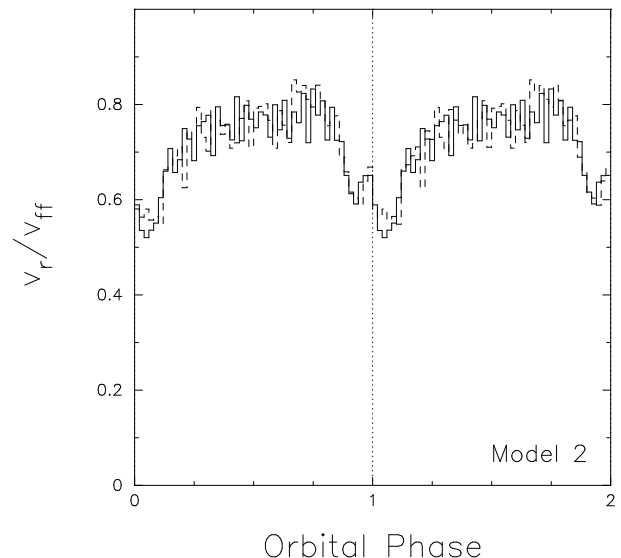


**Fig. 10.** Orbital dependence of the radial velocity normalized by the free-fall velocity at the inner boundary,  $r_{\text{acc}} = 0.2a$ .

enhanced. Although a number of models has been proposed during the last two decades since then (Lehto & Valtonen 1996; Katz 1997; Valtaoja et al. 2000), no widely accepted mechanism has been yet proposed for the behavior of periodic outbursts in OJ287. Furthermore, it has been known that several quasars often show periodic outbursts similar to those in OJ287. The existence of supermassive BBHs has been also suggested for these sources, for example, 3C279 (Abraham & Carrara 1998), PKS 0420-014 (Britzen et al. 2001) and 3C345 (Lobanov & Roland 2005). Such periodic behaviors in the observed light curves of these sources could be also explained by our scenario i.e., the outbursts are driven by the orbital eccentricity of BBHs in three-disk systems, as shown in the lower right panel of Fig. 8 and Fig. 9.

Multiwavelength longterm monitoring observations should be a powerful tool to probe the existence of the circumbinary disks, as well as that of supermassive BBHs. As described in Section 5.1, the photon emerging from the inner region of the disk exhibits different SEDs and their time variations from those emerging from the outer region. In addition, it is expected that the shock-induced radiation should also show periodic variations with the different phase from those of SEDs as seen in Fig. 10. If we detect periodic time variations of SEDs with the different behavior at different wavelengths, it strongly implies the observational evidence for the existence of supermassive BBHs in three-disk systems on a parsec/subparsec scale of the galactic center.

Finally, we give a remark on the quasi-periodicities in the light curves. These are often found in the blazar light curves (see, e.g., Kataoka et al. 2003). In this context, it is interesting to note that Negoro, Mineshige (2002) have found quasi-periodic light variations through the analysis of X-ray intensity variations from Cygnus X-1. It is well known that its X-ray curves are composed of numer-

ous shots (or mini-flares) with a variety of flare amplitudes. By picking up only large shots they found that the light variations follow log-normal distribution. That is, if only large flaring events in the accretion flow produce blob outflow in the form of a jet, jet light curves will be quasi-periodic. This gives another possibility to produce quasi-periodicities in blazar light curves. Much more work is desirable both theoretically and observationally in this area.

## 6. Conclusions

For the purpose of providing the observable diagnosis to probe the existence of supermassive BBHs on a sub-parsec scale of merged galactic nuclei, we have carried out the SPH simulations of accretion flows from circumbinary disks onto the supermassive BBHs. Our main conclusions are summarized as follows:

- (1). There are two-stage mechanisms to cause an accretion flow from the circumbinary disk onto the supermassive BBHs: First, the gas is guided to the two points on the semi-minor axis of the circumbinary disk by the tidal deformation of the circumbinary disk. Then, the gas is increasingly accumulated on these two points by the gravitational attraction of black holes. Second, when the gas can pass across the maximum loci of the binary potential, the gas overflows via these two points and freely infalls onto each black hole.
- (2). In circular binaries, the gas continues to be supplied from the circumbinary disk onto the supermassive BBHs (i.e. the gap is always closed)
- (3). In eccentric binaries, there is the material supply with the periodic on/off transitions during one orbital period because of the time-dependent, periodic potential.
- (4). While the mass-capture rates exhibit little orbital-phase dependence in circular binaries, it significantly modulates with the orbital phase due to the gap opening/closing cycles, in eccentric binaries. This could provide the observable diagnosis for the presence of supermassive BBHs in three-disk systems at the galactic center.
- (5). The circumbinary disks are formed around each black hole regardless of the orbital eccentricity and the mass ratio.

K.H. is grateful to Noboru Kaneko, Atsuo T. Okazaki, James R. Murray, Yasuhiro Asano and Satoshi Tanda for their continuous encouragement. K.H. is also grateful to Atsuo T. Okazaki, Jun Fukue and Shoji Kato for helpful discussions. The simulations reported here were performed using the facility of the Centre for Astrophysics & Supercomputing at Swinburne University of Technology, Australia and of YITP in Kyoto University. This work has been supported in part by the Grants-in-Aid of the Ministry of Education, Science, Culture, and Sport and Technology (MEXT; 14079205 K.H, 16340057 S.M.),

and by the Grant-in-Aid for the 21st Century COE Scientific Research Programs on "Topological Science and Technology" and "Center for Diversity and Universality in Physics" from the MEXT.

## References

Abraham, Z., & Carrara, E.A. 1998, ApJ, 496, 172  
 Armitage, P.J & Natarajan, P. 2002, ApJ, 567, L9  
 Armitage, P.J & Natarajan, P. 2005, ApJ, 634, 921  
 Artymowicz, P. 1998, in Theory of Black Hole Accretion Discs, ed. Abramowicz, M.A., Björnsson, G., & Pringle, J.E. (Cambridge: Cambridge University Press), 202  
 Artymowicz, P., Clarke, C.L., Lubow, H.S., & Pringle, J.E. 1991, ApJ, 370, L35  
 Artymowicz, P., & Lubow, H.S. 1994, ApJ, 421, 651  
 Artymowicz, P., & Lubow, H. S. 1996, ApJ, 467, L77  
 Artymowicz, P., & Lubow, H.S. 1996, In Disks and Outflows around Young Stars, ed. Beckwith, S., Staude, J., Quetz, A., & Natta, A. (Berlin, Heidelberg and NewYork: Springer-Verlag), 115  
 Bate, M. R., Bonnel, I. A., & Price, N.M. 1995, MNRAS, 277, 362  
 Bate, M. R., & Bonnel, I.A. 1997, MNRAS, 285, 33  
 Begelman, M.C., Blandford, R.D., & Rees, M.J. 1980, Nature, 287, 307  
 Benz W. 1990, in the Numerical Modeling of Nonlinear Stellar Pulsations: Problems and Prospects, ed. Buchler, R.J. (Dordrecht: Kluwer Academic Publishers), 269  
 Benz, W., Bowers, R.L., Cameron, A.G.W., & Press, W.H. 1990, ApJ, 348, 647  
 Britzen, S., Roland, J., Laskar, J., Kokkotas, K., Campbell, R.M., & Witzel, A. 2001, A&A, 374, 784  
 Di Matteo, Tiziana, Springel, V., & Hernquist, L. 2005, Nature, 433, 604  
 Ferrarese Laura & Merritt David 2000, ApJ, 539, L9  
 Günther, R. C., & Kley, W. 2002, A&A, 387, 550  
 Günther, R. C & Kley, W. 2004, A&A, 423, 559  
 Gebhardt K et al 2000, ApJ, 539, L13  
 Hayasaki, K., & Okazaki, A.T. 2004, MNRAS, 467, 77  
 Hayasaki, K., & Okazaki, A.T. 2005, MNRAS, 360, L15  
 Hayasaki, K., & Okazaki, A.T. 2006, MNRAS, in press  
 Kauffmann, G.,& Haehnelt, M. 2000, MNRAS, 311, 576  
 Kataoka, J., et al. 2003, ApJ, 560, 659  
 Kato, S., Fukue, J., & Mineshige, S. 1998, Black-Hole Accretion Disks (Kyoto: Kyoto University Press)  
 Katz, J.I. 1997, ApJ, 478, 527  
 Kitamura, S. 1970, Ap&SS, 7, 272  
 Kormendy, J., & Richstone, D. 1995, ARA&A, 33, 581  
 Komossa, S. 2003, Observational Evidence for Supermassive Black Hole Binaries, ed. Centrella, J.M (AIP Conference Proceedings), 161  
 Komossa, S. 2006, Memorie della Societa Astronomica Italiana, 77, 733  
 Lehto, H.J., & Valtonen, M.J. 1996, ApJ, 460, 207  
 Lobanov, A.P., & Roland, J. 2005, A&A, 431, 831  
 Lubow, H. S., & Artymowicz, P. 1996, In Evolutionary Processes in Binary Stars, ed. Ralph, A.M., Wijers, J., Melvyn, B.D (Dordrecht: Kluwer Academic Publishers), 53  
 Lubow H. S., & Artymowicz, P. 2000, In Protostars and Planets IV, ed. Mannings, V., Boss, A.P., & Russell, S.S. (Tucson: University of Arizona Press), 731  
 Lynden-Bell, D. 1969, Nature, 223, 690

Makoto Miyoshi, James Moran, James Herrnstein, Lincoln Greenhill, Naomasa Nakai, Phillip Diamond., Makoto Inoue 1995, *Nature*, 373, 127

Negoro, H.,& Mineshige, S. 2002, *PASJ*, 54, L69

Maness, H.L., Taylor, G.B., Zavala, R.T., Peck, A.B., & Pollack, L.K. 2004, *ApJ*, 602, 123

MacDonald, G.J.F. 1964, *Rev.Geophys*, 2, 467

MacFadyen, A.I., & Milosavljević, M. 2006, *astroph/0607467*

Meglicki Z, Wickramasinghe D, Bicknell G 1993, *MNRAS*, 264, 691

Merritt David 2006, *astroph/0605070*

Merritt, D & Ekers, R.D. 2002, *Science*, 297, 1310

Milosavljević, M., & Merritt, D. 2001, *ApJ*, 563,34

Monaghan J.J & Gingold 1983, *J.Comput.Phys*, 52, 374

Murray, C.D., & Dermott, S.F. 1999, *Solar System Dynamics* (Cambridge: Cambridge University Press), ch.4, 160

Murray, J.R. 1998, *MNRAS*, 297, 323

Okazaki, A.T., Bate, M.R., Ogilvie, G.I., & Pringle J.E. 2002, *MNRAS*, 337, 967

Ochi Y, Sugimoto K & Hanawa T 2005, *ApJ*, 623, 922

Papaloizou, J., & Pringle, J.E. 1977, *MNRAS*, 181, 441

Polnarev, A.G., & Rees, M.J. 1994, *A&A*, 283, 301

Quinlan, G., & Hernquist, L. 1997, *New Astron*, 2, 533

Rauch, K., & Tremaine, S. 1996, *New Astron*, 1, 149

Rees M.J 1984, *ARA&A*, 22, 471

Rodriguez C et al 2006, *astroph/0604042*

Roos, N. 1981, *A&A*, 104, 218

Roos, N., Kaastra, J.S., & Hummel, C.A. 1993, *ApJ*, 409, 130

Shakura, N.I., & Sunyaev, R.A. 1973, *A&A*, 24, 337

Silk, J., & Rees, M.J. 1998, *A&A*, 331, L1

Sillanpää, A., Haarala, S., Valtonen, M., Sundelius, B., & Byrdi, G.G. 1988, *ApJ*, 325, 628

Stothers, R.B., & Sillanpää, A. 1997, *ApJL*, 475, L13

Sudou, H., Iguchi, S., Muratai, Y., & Taniguchi, T. 2003, *Science*, 300, 1263

Tanaka, Y., et al. 1995, *Nature*, 375, 659

Valtaoja, E., et al. 2000, *ApJ*, 531, 744

Valtonen, M.J., et al. 2006, *ApJL*, 643, L9

Yu, Q. 2002, *MNRAS*, 331, 935